Supplementary Information

Dynamic signatures of electronically nonadiabatic coupling in sodium hydride: a rigorous test for the symmetric quasi-classical model applied to realistic, *ab initio* electronic states in the adiabatic representation

Justin J. Talbot[1*], Martin Head-Gordon[1,2], William H. Miller[1], and Stephen J. Cotton[1]

[1]Department of Chemistry, University of California, Berkeley, California 94720, United States

[2]Chemical Sciences Division, Lawrence Berkeley National Laboratory, Berkeley, California, 94720, United States

[*]Corresponding author. Email: justin.talbot@berkeley.edu

Table of Contents

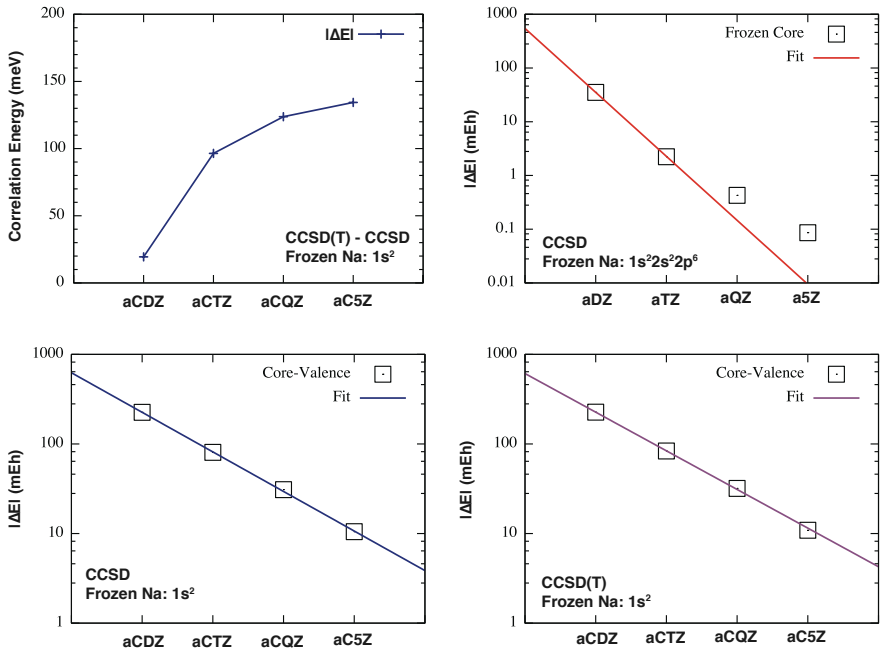

Fig. S1: Convergence tests of the ground electronic state correlation energy as a function of increasing basis set. The absolute deviation between CCSD(T) and CCSD correlation energy (**top, left**). The incremental change in correlation energy from the frozen-core basis sets (**top, right**). The incremental change in correlation energy from the core-valence polarized basis sets with the CCSD (**bottom, left**) and CCSD(T) (**bottom, right**) methods.

1 Electronic Structure Analysis

1.1 Ground Electronic State Correlation Energy

Convergence of the ground electronic state ($\mathbf{X}^1\Sigma^+$) correlation energy with respect to basis set was tested using a series of aug-cc-p(C)VnZ (denoted a(C)nZ, n = D, T, Q, 5) basis sets that included both frozen-core and core-valence polarized basis functions. The frozen core was defined as the $1s^2 2s^2 2p^6$ electrons from the sodium atom. For the core-valence polarized basis sets, only the $1s^2$ orbitals on the sodium atom are excluded from the correlated calculations. The bond length of sodium hydride was optimized using restricted CCSD with the aCV5Z core-valence polarized basis set ($\mathbf{R} = 1.8910$Å).

As shown in Fig. S1A, including perturbative triple excitations lowers the correlation energy by 124 meV at the quadruple-zeta level which is only 10 meV higher than the quintuple-zeta correction (134 meV). The incremental change[1] in correlation energy how-

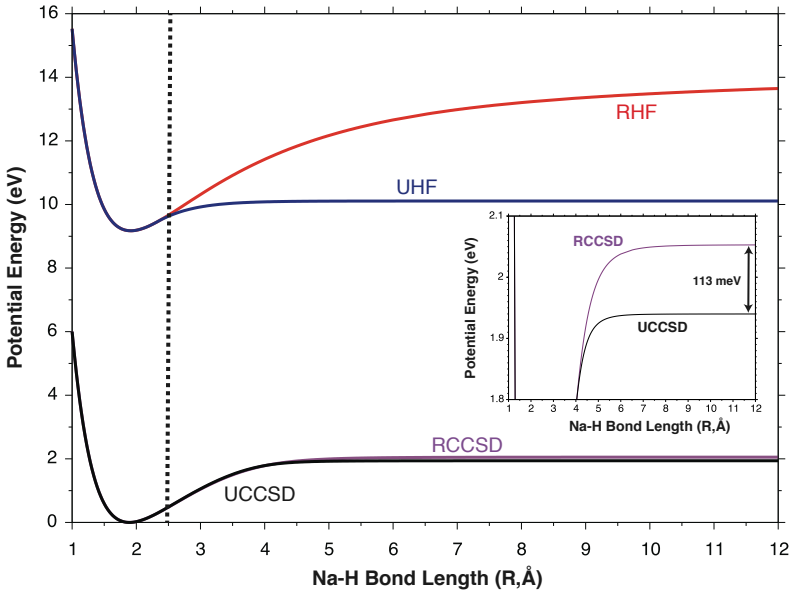

Fig. S2: The CCSD ground state potential energy surface calculated with unrestricted (**black**, UCCSD) and restricted (**purple**, RCCSD) Hartree-Fock orbitals. The unrestricted (**blue**, UHF) and restricted (**red**, RHF) Hartree-Fock potential energy surfaces. The dashed vertical line is the bond length of the Coulson-Fischer point. The energy splitting between the RCCSD and UCCSD dissociation energies (**inset**).

ever, shows that the frozen core approximation significantly underestimates the correlation energy introducing substantial deviations from correlation consistency which is particularly problematic for the quadruple- and quintuple-zeta basis sets (see Fig. S1B). Correlation consistency is obtained when the sodium atoms $2s^2 2p^6$ electrons are correlated (see Fig. S1C). Likewise, correlation consistency is maintained, with the core-valence polarized basis sets, when perturbative triple excitations are included (see Fig. S1D).

All potential energy surface calculations in this work employed restricted Hartree-Fock orbitals as a basis when solving the coupled-cluster equations. This basis was chosen because restricted orbitals provide spin-pure eigenstates beyond the Coulson-Fischer point allowing for greater computational efficiency as less EOM-EE-CCSD roots are required. For a general molecular system, this choice of basis could lead to an increased dissociation limit for the ground electronic state as the electronic wavefunction takes on multi-configurational character; however, for two-electrons CCSD is formally exact and Ref. [2] has provided compelling evidence that NaH can be accurately modeled as an effective two-electron sys-

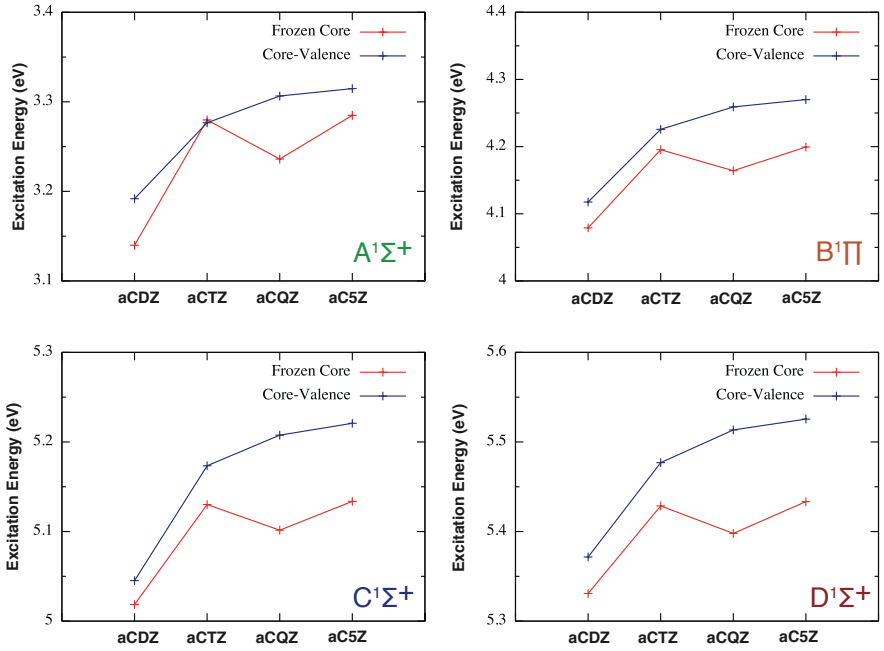

Fig. S3: EOM-EE-CCSD excitation energies for the **A**, **B**, **C**, and **D** excited electronic states with increasing basis set referenced from the ground electronic state equilibrium bond length. Comparisons are made between frozen-core basis sets (**red**) and core-valence correlated basis sets (**blue**).

tem. Assuming this is the case for NaH, the RCCSD and UCCSD ground electronic state energies would dissociate to the same limit even though the RHF dissociation energy will be significantly higher than UHF. As shown in Fig. S2, there is some lowering of the ground state energy using unrestricted orbitals (113 meV at $\mathbf{R} = 12$ Å) beyond the Coulson-Fischer point; however, restricted orbitals still capture most of the correlation energy and therefore provide an adequate basis for the excited state calculations. While only problematic beyond the Coulson-Fischer point, the use of restricted orbitals as a basis can result in numerical instabilities and ill-convergence when solving the coupled-cluster equations. Although current options are limited, the convergence problems could potentially be corrected with a more robust numerical solver and NaH could be a useful test system for developing such algorithms.

Table S1: Calculated Rydberg energies with the frozen-core and core-valence polarized basis sets. The experimental values for the $3p$ and $4p$ Rydberg energies are averaged over the fine structure.

	Frozen-Core			Core-Valence		
Basis	**3p**	**4s**	**4p**	**3p**	**4s**	**4p**
DZ	1.979	3.059	3.593	2.010	3.084	3.632
TZ	1.978	3.056	3.594	2.063	3.150	3.703
QZ	1.973	3.053	3.599	2.079	3.168	3.730
5Z	1.973	3.053	3.588	2.088	3.179	3.734
Experiment	2.103	3.191	3.753	2.103	3.191	3.753

1.2 Excited Electronic State Energies

Convergence tests of the **A**, **B**, **C**, and **D** excited electronic state energies were also performed at the EOM-EE-CCSD level using the same correlation consistent core-valence and frozen-core basis sets (see Fig. S3). The excitation energies were referenced from the ground electronic state equilibrium bond length optimized with the aCV5Z basis set. Across the correlation consistent series, the frozen-core basis sets systematically underestimate all excitation energies when compared with their core-valence counterparts. Likewise, the frozen-core basis sets introduce a distinct kink in the excitation energies at the quadruple-zeta level hindering convergence to the complete basis set limit. Smooth convergence to this limit is obtained with the core-valence polarized basis sets.

1.3 Rydberg States

In addition, the $3p$, $4s$, and $4p$ Rydberg energies of the sodium atom Na(I) ($^2S_{1/2}$) were calculated as an additional convergence test and compared against experimental values.[3] The absolute errors calculated with the frozen-core and core-valence polarized basis sets are shown in Fig. S4 with the Rydberg energies provided in table S1. Since spin-orbit coupling was not included in the electronic structure calculations, the experimental $J = 1/2$ and $J = 3/2$ fine structure measurements of the $3p$ and $4p$ Rydberg excitations were averaged for comparison with the calculated values. For all tested Rydberg excitations the quadruple- and quintuple-zeta basis sets have absolute errors below 0.03 eV (the dashed line in Fig. S4). Since the errors at the quadruple-zeta level (aCQZ) are tolerable, and after considering the

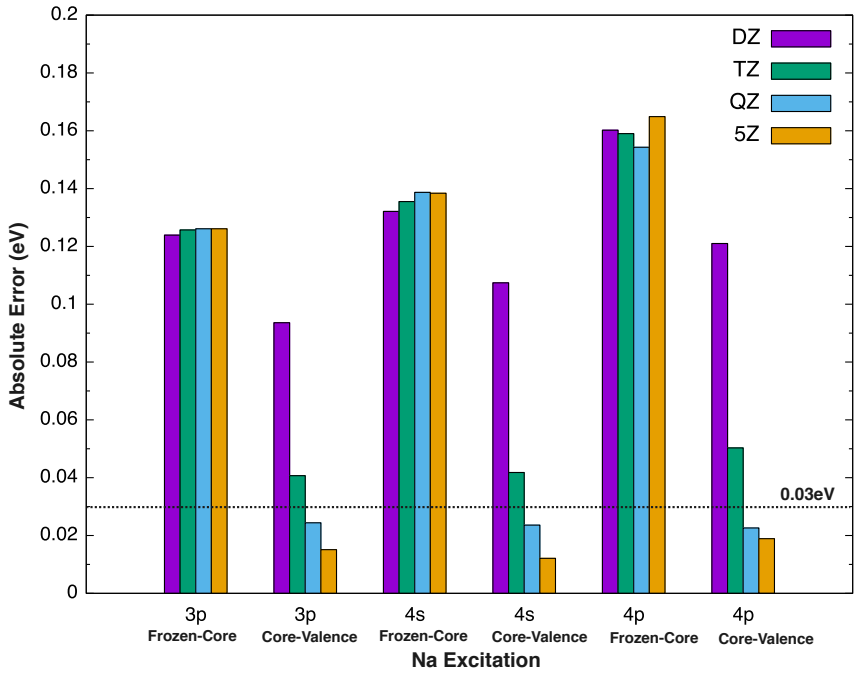

Fig. S4: Absolute error between the calculated and experimental values of the $3p$, $4s$, and $4p$ Rydberg excitations of the sodium atom ($^2S_{1/2}$).

convergence tests in sections 1.1 and 1.2, this basis was chosen for all electronic structure calculations.

1.4 Comparison with Previously Reported Potentials

To further demonstrate convergence of the electronic structure, a comparison between the potential surfaces calculated here and those calculated by Aymar, Deiglmayr, and Dulieu[2] is provided in Fig. S5. While the dissociation limit of the ground electronic state calculated with RCCSD/aCQZ is elevated in comparison (see section 1.1), there is very good agreement between the calculated excited state potential energy surfaces from the two studies. For a detailed assessment of the accuracy of the **X**, **A**, and **C** potential energy surfaces provided by Ref. [2], including corrections using experimentally measured parameters, see Ref. [4] and Ref. [5].

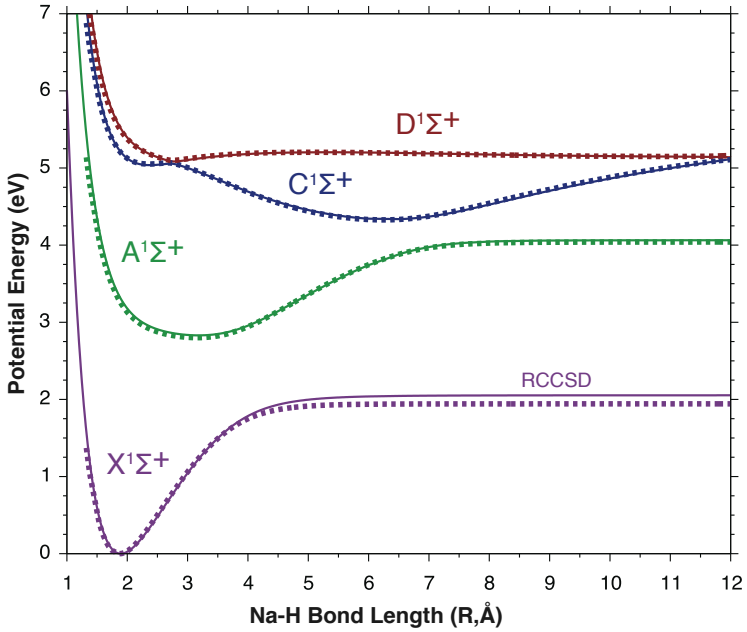

Fig. S5: A comparison between the **X**, **A**, **C**, and **D** potential energy surfaces calculated using RCCSD and EOM-EE-CCSD with the aCQZ basis (**solid lines**, this work) and those provided by Ref. [2] (**dashed lines**).

2 Vibronic Energy Level Analysis

2.1 Extrapolated Potential Energy Surfaces

As discussed in the main text, the grid was truncated at $\mathbf{R} = 12$Å as convergence of the coupled-cluster T-amplitudes was problematic in this region. The analysis below provides estimates for the error in the quantum mechanical calculations that result from truncating the grid at this bond length. Convergence with respect to grid was tested by extrapolating the **A**, **C**, and **D** potential energy surfaces, and corresponding first-order derivative couplings, out to $\mathbf{R} = 20$Å followed by recomputing the vibronic energy levels and quantum population dynamics on the extrapolated grid. The truncated grid, referred to below, is the same grid that was used for all calculations in the main text.

The extrapolated region is defined as $\mathbf{R} > 12$Å with functional forms for the potential energy surfaces for $\mathbf{R} > 12.5$Å. In the intermediate region, between $12\text{Å} < \mathrm{R} < 12.5\text{Å}$, a linear interpolation was performed. For the potential energy surfaces, the **A** and **C** surfaces

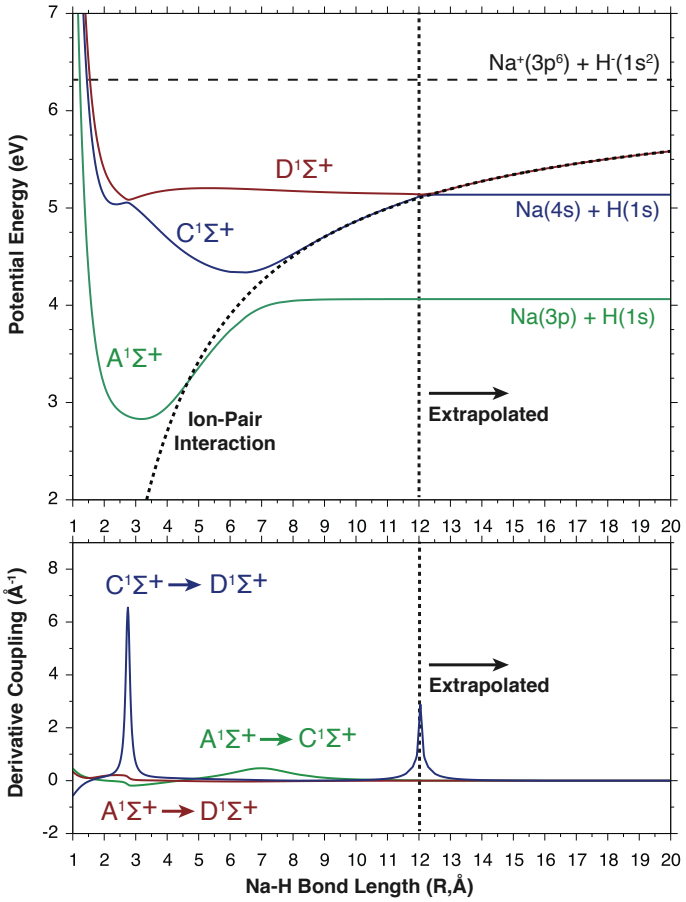

Fig. S6: The extrapolated **A**, **C**, and **D** potential energy surfaces with the corresponding first-order derivative couplings used for the grid convergence tests.

were simply set to a constant value in the extrapolated region and the **D** surface was set to follow the ion-pair interaction energy. The potential energy surfaces in the extrapolated region are shown in the top panel of Fig. S4 with their functional forms given by Eqs. 1a-c:

$$V_A(\mathbf{R}) = V_A(\mathbf{R} = 12) \qquad \mathbf{R} > 12.5\text{Å} \tag{1a}$$

$$V_C(\mathbf{R}) = V_D(\mathbf{R} = 12) \qquad \mathbf{R} > 12.5\text{Å} \tag{1b}$$

$$V_D(\mathbf{R}) = -\frac{1}{\mathbf{R}} + 6.303 \qquad \mathbf{R} > 12.5\text{Å} \tag{1c}$$

where 6.303 eV is the CCSD/aCQZ ion-pair dissociation limit.

Extrapolation of the first-order derivative coupling functions was performed by setting the **A**-**C** and **A**-**D** couplings to zero in the extrapolated region. The **C**-**D** first-order derivative coupling was extrapolated by reflecting the coupling around $\mathbf{R} = 12$Å (see bottom panel of Fig. S4). The linearly-interpolated grid spacing (0.015Å) was used for all extrapolations. On the extrapolated grid there are $3,597$ total basis functions with $1,199$ attributed to each adiabatic state.

2.2 Quantum Dynamics

The Fourier-grid Hamiltonian method enforces periodic boundary conditions which are preferable when solving for the eigenfunctions of Hamiltonians containing unbound potential energy surfaces. For the quantum dynamics, no further boundary conditions (e.g., absorbing potentials) where enforced. Instead, only short-time dynamics were simulated ($t <= 60$ fs) such that the simulations at each pump-probe delay time (δ) were terminated before the wavepacket reached the boundary. This is demonstrated in Fig. S7 where the population transfer after excitation to the **C** state ($\delta = 0$ fs) is compared for long time dynamics ($t = 200$ fs) between the truncated and extrapolated grids. For $t <= 80$ fs there is no discernible difference in the population transfer using either grid.

To show that the population transfer is unaffected at longer pump-probe delay times,

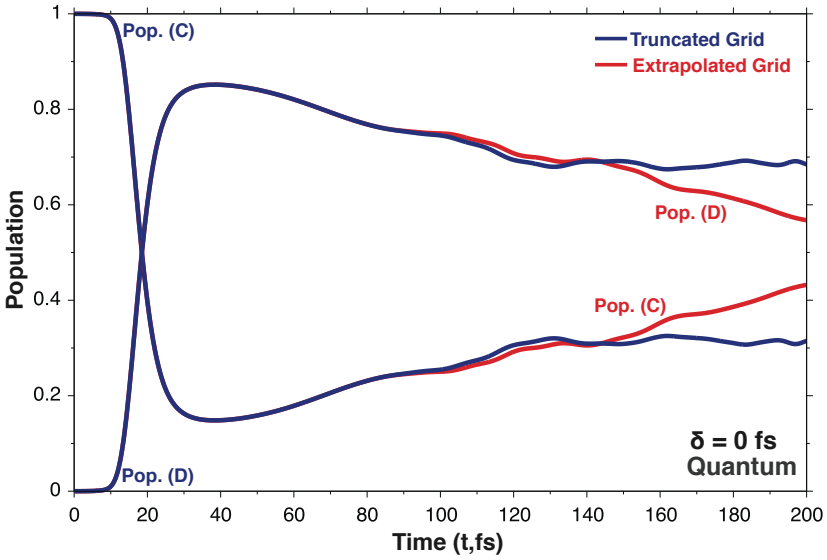

Fig. S7: The long-time quantum population dynamics ($\delta = 0$) calculated on the truncated (blue) and extrapolated (red) grids after initial excitation to the **C** adiabatic state.

the quantum dynamics were simulated analogous to Figs. 4-8 in the main text on the extrapolated grid. Comparisons between the population transfer on the truncated and extrapolated grids are shown in Fig. S8 and Fig. S9. The error, which is defined as the signed difference between the truncated and extrapolated populations, is shown in the right panel of each figure. The MAD between the left and middle plots was also calculated. For population transfer after excitation to the **C** state (Fig. S8) the maximum signed error is -0.02 and the MAD is 1.79e$-$4. For population transfer after excitation to the **D** state (Fig. S9) the MAD is 1.32e$-$4.

2.3 Adiabatic Vibronic Energy Levels

A comparison between select adiabatic ($\mathbf{d}_{ij}(\mathbf{Q}) = 0$) vibrational energy levels calculated on the truncated and extrapolated grids near the avoid crossing region is provided in Table S2 with an energy level diagram shown in Fig. S10. The error is defined as the signed energy difference between vibrational states from the truncated and extrapolated grids. For vibrational levels on the **C** adiabat, the error systematically increases with quantum number reaching 0.006 eV for the highest energy bound state (**C**,42). On the extrapolated

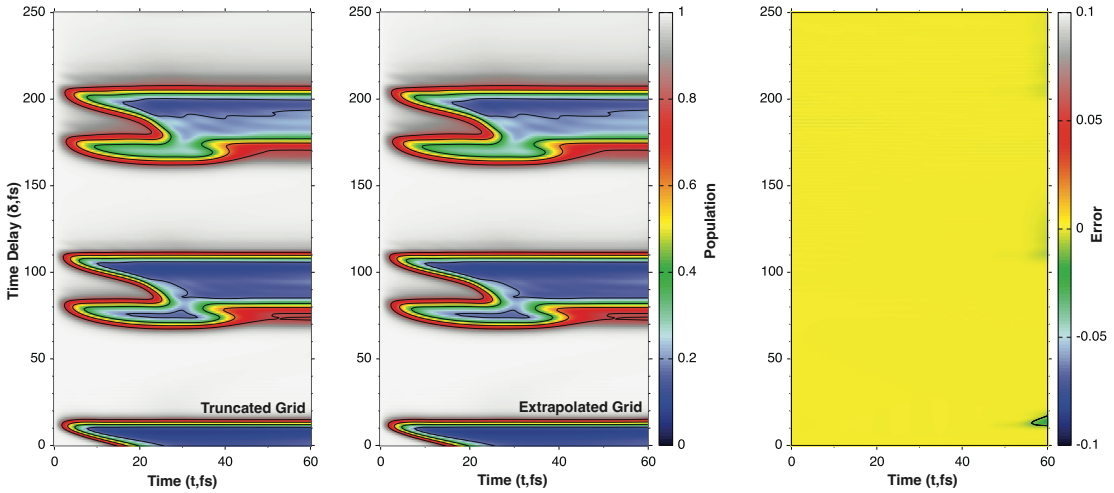

Fig. S8: A comparison between the quantum population dynamics calculated on the truncated (**left**) and extrapolated (**middle**) grids after initial excitation to the **C** state. The contour lines in the left and middle panels represent a decrease in population of 0.2. The signed difference between the quantum population dynamics calculated on the truncated and extrapolated grids (**right**). The contour lines represent a signed error of ±0.01.

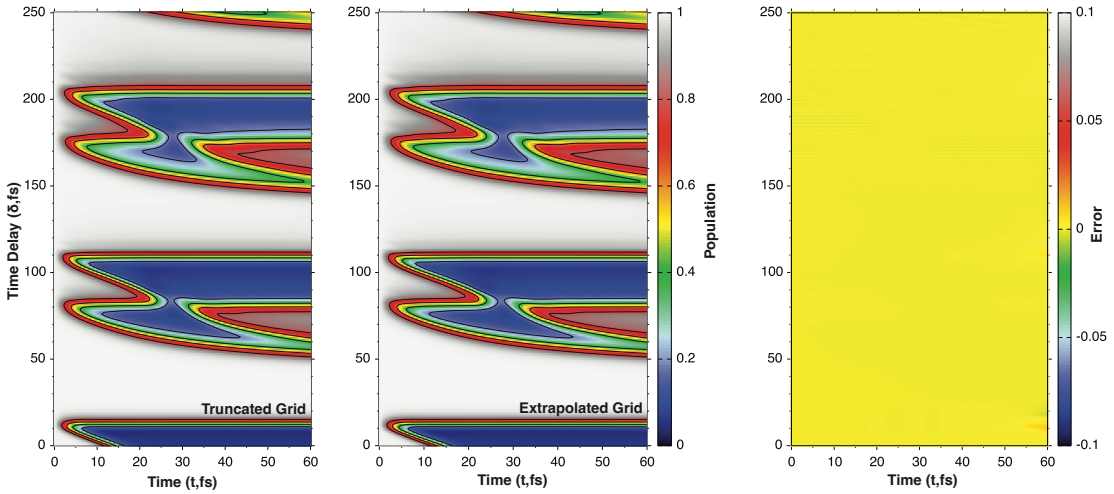

Fig. S9: A comparison between the quantum population dynamics calculated on the truncated (**left**) and extrapolated (**middle**) grids after initial excitation to the **D** state. The contour lines in the left and middle panels represent a decrease in population of 0.2. The signed difference between the quantum population dynamics calculated on the truncated and extrapolated grids (**right**). All signed errors are below ±0.01.

Table S2: A comparison between select adiabatic ($\mathbf{d}_{ij}(\mathbf{Q}) = 0$) vibronic energy levels near the avoided crossing region calculated on the truncated and extrapolated grids. The unbound vibronic state (**C**,43) is shown for reference.

	Truncated Grid	Extrapolated Grid	
State (Φ, χ)	**Energy (eV)**	**Energy (eV)**	**Difference**
		$C^1\Sigma^+$	
C,34	5.037	5.037	0.000
C,35	5.051	5.051	0.000
C,36	5.061	5.061	0.000
C,37	5.071	5.071	0.000
C,38	5.084	5.084	0.000
C,39	5.098	5.097	0.001
C,40	5.112	5.110	0.002
C,41	5.126	5.123	0.003
C,42	5.140	5.134	0.006
C,43	5.155	5.137	0.018
		$D^1\Sigma^+$	
D,0	5.116	5.116	0.000
D,1	5.151	5.147	0.004
D,2	5.159	5.155	0.004
D,3	5.160	5.160	0.000
D,4	5.167	5.162	0.005
D,5	5.175	5.169	0.006
		MAD (eV):	0.003

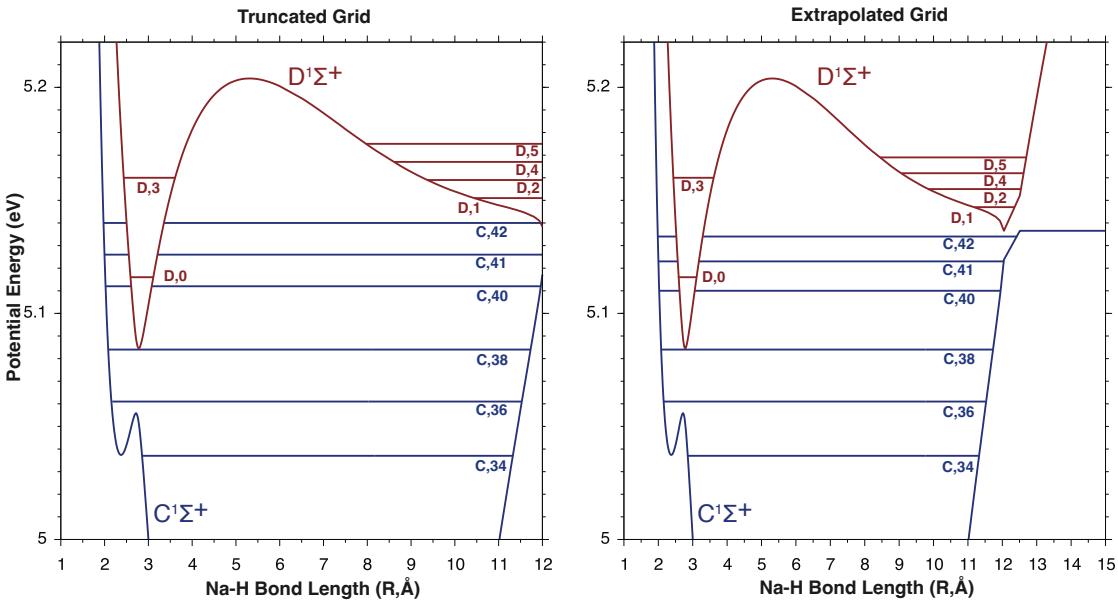

Fig. S10: An energy level diagram of select adiabatic vibronic energy levels near the avoided crossing region calculated on the truncated (**left**) and extrapolated (**right**) grids.

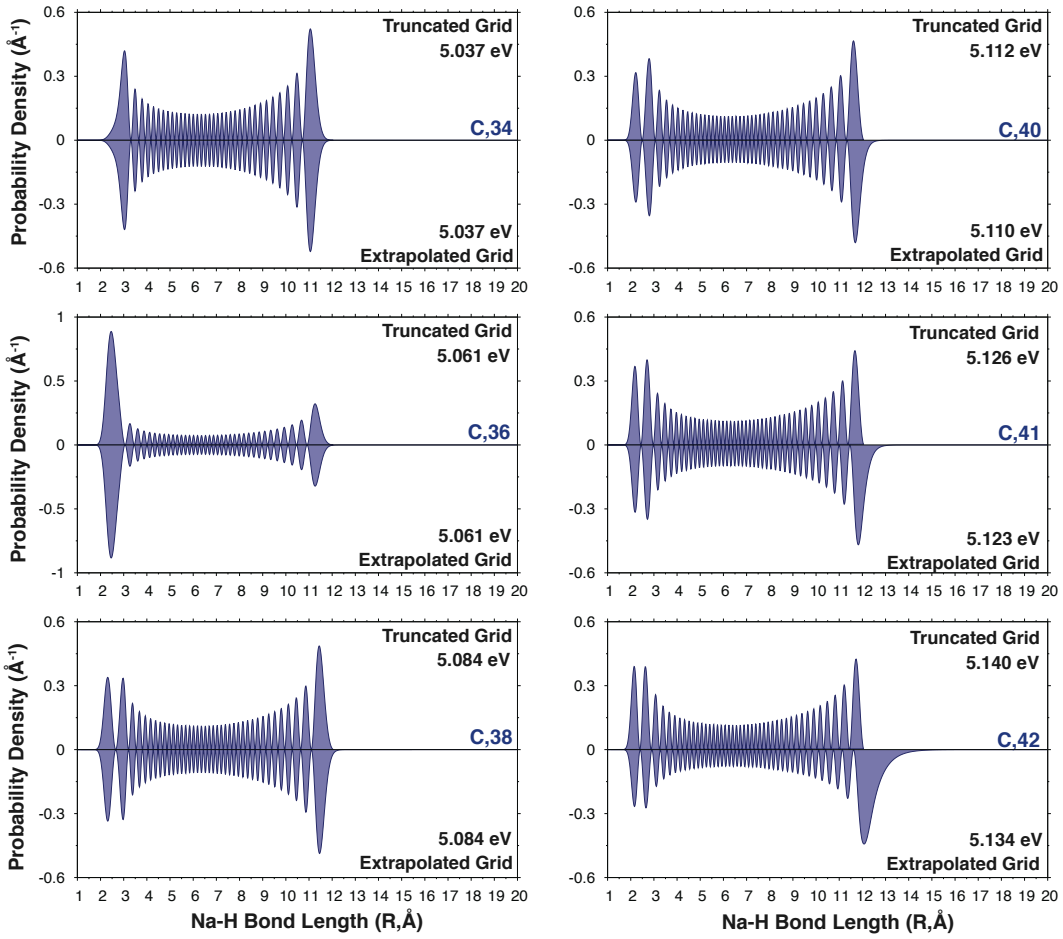

Fig. S11: A comparison between select adiabatic probability densities from the **C** state calculated on the truncated (**top**) and extrapolated (**bottom**) grids.

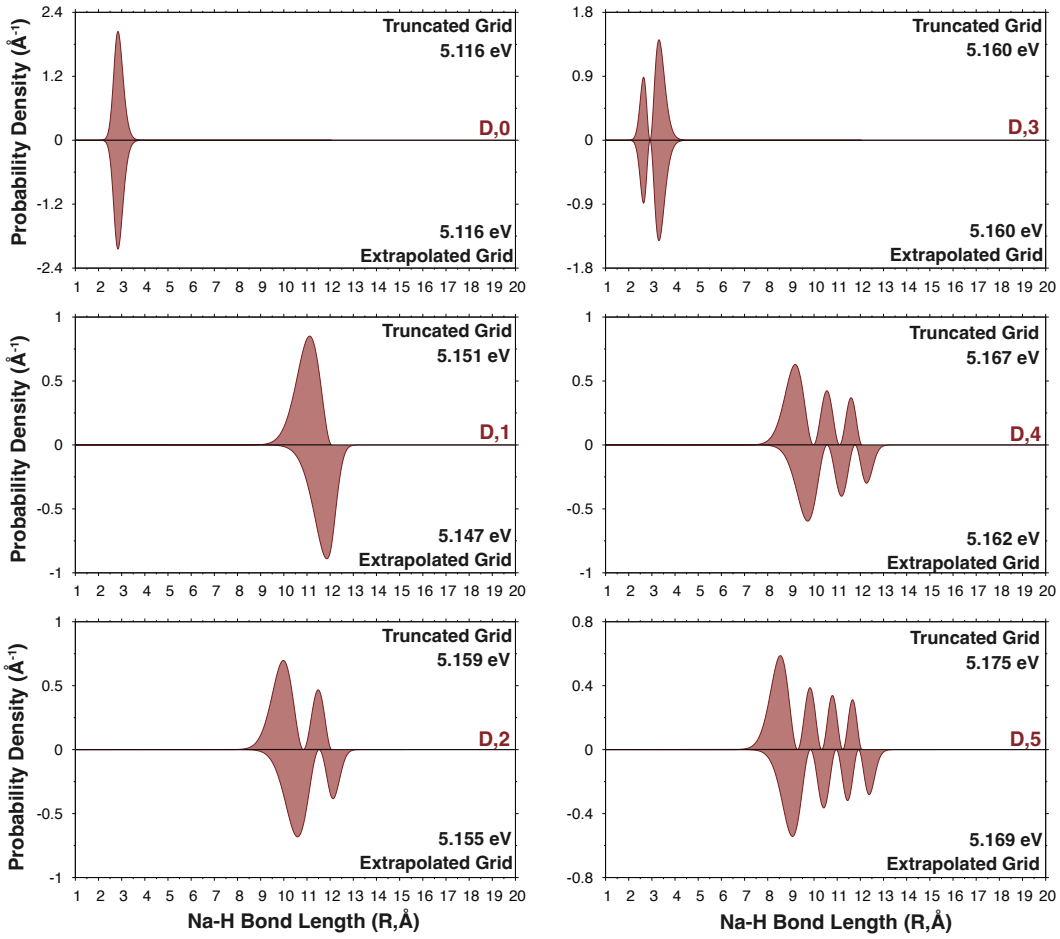

Fig. S12: A comparison between select adiabatic probability densities from the **D** state calculated on the truncated (**top**) and extrapolated (**bottom**) grids.

C potential energy surface, the dissociation threshold was set at 5.136 eV which is just below the energy of the **C**,43 vibronic state (5.137 eV). While this results in an unbound **C**,43 state, the energy is close enough to the dissociation threshold to be within the error of the method. Select vibrational probability densities from the **C** adiabat are also provided in Fig. S11. Unsurprisingly, for vibrational levels greater than **C**,39 the probability densities from the extrapolated grid extend to longer bond lengths when compared with the truncated grid contributing the primary source of error. For vibrational levels less than **C**,39, there is no discernible difference between the probability densities from the two grids.

Interestingly, the **D** potential energy surface also forms a double-well with a sufficiently high barrier that localizes low-lying eigenstates. As shown in Table S2, the adiabatic vibrational states localized around shorter bond lengths, **D**,0 and **D**,3, are well converged with the truncated grid and the error for adiabatic eigenstates localized around longer bond lengths increases with quantum number. For **D** vibrational states in this region the maximum error is again 0.006 eV which arises from the **D**,5 state. Select adiabatic probability densities from the **D** adiabat are also provided in Fig. S12 which further show that the vibrational eigenstates are converged when localized around shorter bond lengths (**D**,0 and **D**,3). For vibrational eigenstates that are localized around longer bond lengths, the probability densities look qualitatively similar but the densities on the extrapolated grid extend further into the extrapolated regime.

2.4 Nonadiabatic Vibronic Energy Levels

A comparison between select nonadiabatically coupled ($\mathbf{d}_{ij}(\mathbf{Q}) \neq 0$) vibronic energy levels calculated on the truncated and extrapolated grids near the avoided crossing region is provided in Table S3 with an energy level diagram shown in Fig. S13. Consistent with the adiabatic vibronic states, the error when nonadiabatic coupling is included increases as the dissociation threshold is approached for vibronic states with primarily **C** character. The error in the highest bound state (**C**,42) is comparable but slightly higher (0.007 eV) than the error in the adiabatic-only calculation (0.006 eV). Even when nonadiabatic coupling is

Table S3: A comparison between the nonadiabatically coupled ($\mathbf{d}_{ij}(\mathbf{Q}) \neq 0$) vibronic energy levels calculated on the truncated and extrapolated grids near the avoided crossing region.

	Truncated Grid		Extrapolated Grid		
State (Φ, χ)	**Energy (eV)**	**Char.**	**Energy (eV)**	**Char.**	**Difference**
			$C^1\Sigma^+$		
C,34	5.038	0.981	5.038	0.980	0.000
C,35	5.053	0.935	5.053	0.921	0.000
C,36	5.063	0.846	5.063	0.847	0.000
C,37	5.069	0.882	5.069	0.752	0.000
C,38	5.083	0.914	5.082	0.914	0.001
C,39	5.097	0.940	5.096	0.940	0.001
C,40	5.110	0.842	5.109	0.884	0.001
C,41	5.128	0.653	5.125	0.641	0.003
C,42	5.143	0.742	5.136	0.658	0.007
C,43	5.160	0.363	5.137	0.926	0.023
			$D^1\Sigma^+$		
D,0	5.116	0.382	5.116	0.371	0.000
D,1	5.152	0.803	5.149	0.517	0.003
D,2	5.159	0.844	5.155	0.728	0.004
D,3	5.151	0.253	5.155	0.150	-0.004
D,4	5.167	0.992	5.162	0.558	0.005
D,5	5.175	0.705	5.169	0.730	0.006
				MAD (eV):	0.004

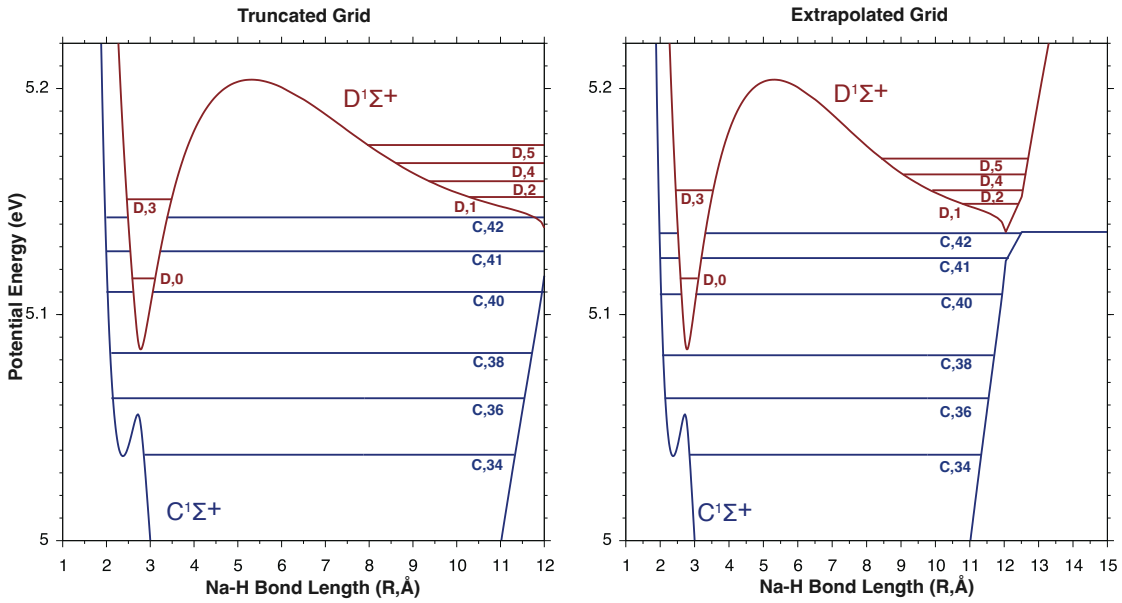

Fig. S13: An energy level diagram of select nonadiabatically coupled vibronic energy levels near the avoided crossing region calculated on the truncated (**left**) and extrapolated (**right**) grids.

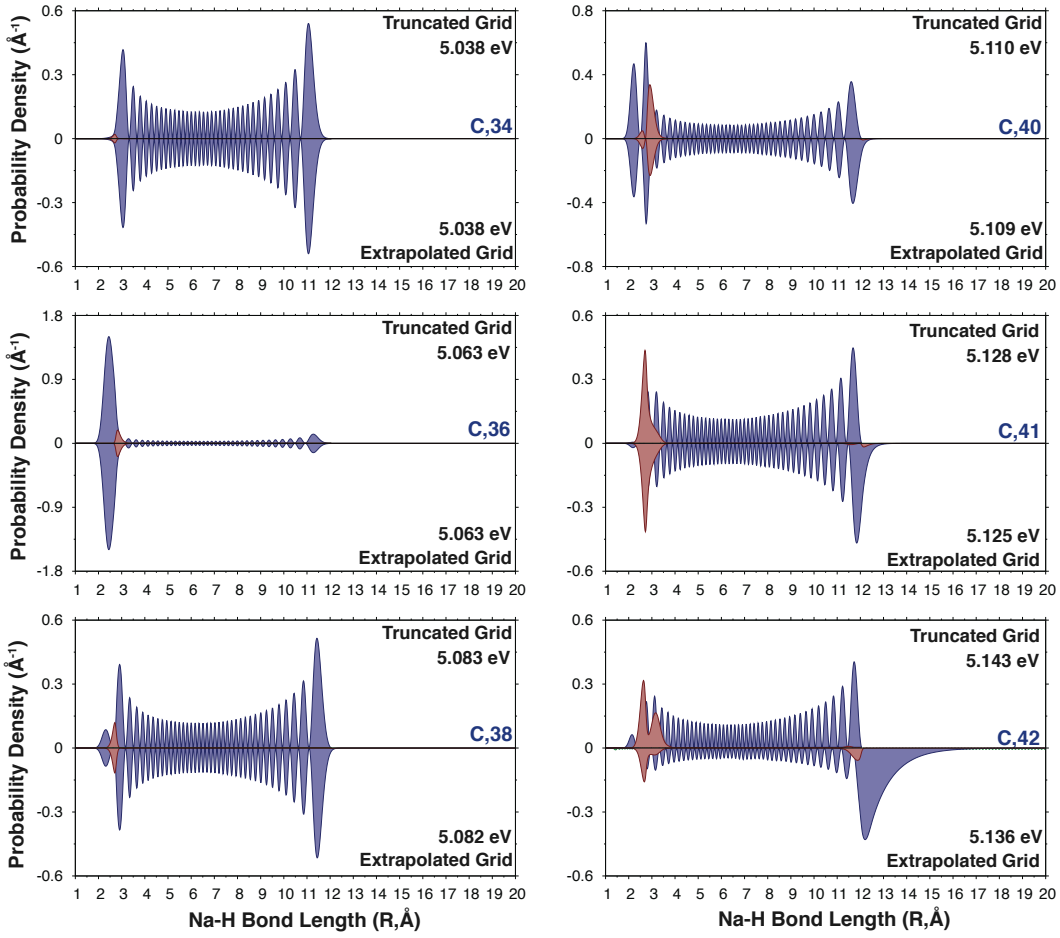

Fig. S14: A comparison between select nonadiabatically coupled probability densities with primarily **C** character calculated on the truncated (**top**) and extrapolated (**bottom**) grids. The **C** state contribution (blue) and **D** state contribution (red) are shown.

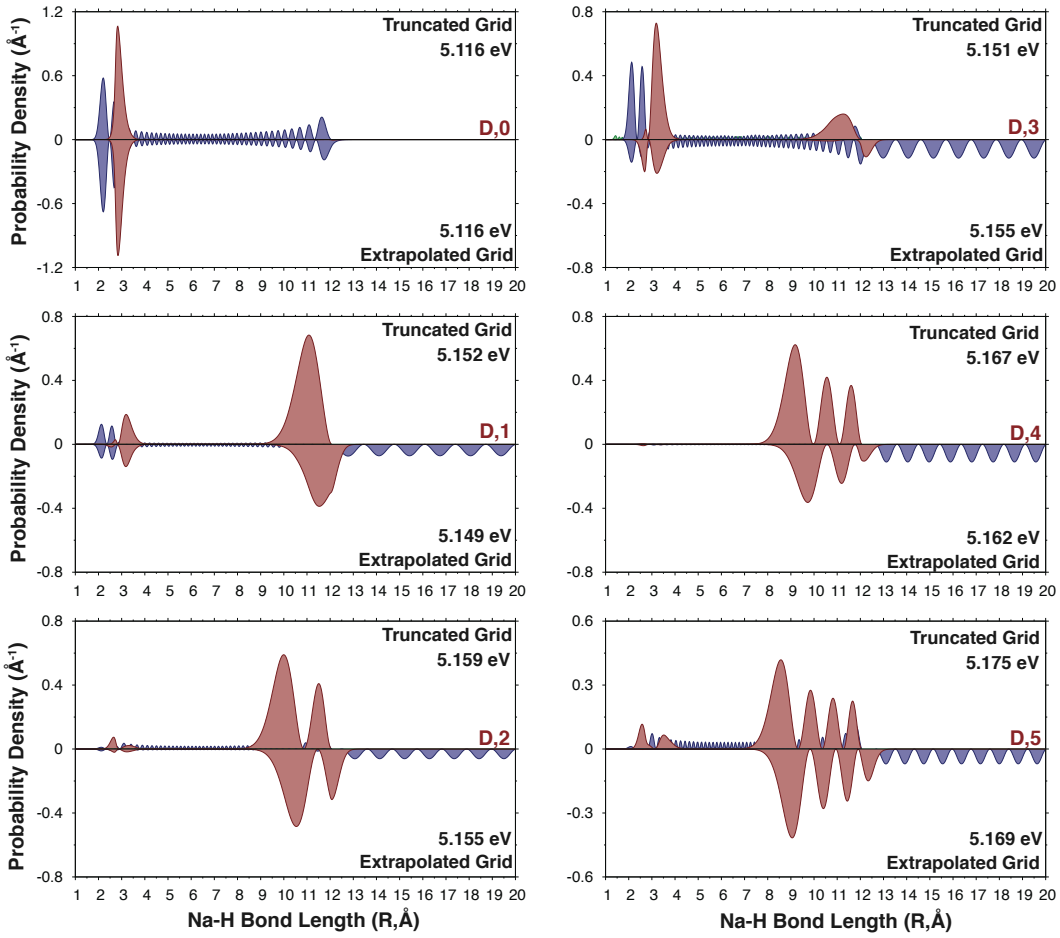

Fig. S15: A comparison between select nonadiabatically coupled probability densities with primarily **D** character calculated on the truncated (**top**) and extrapolated (**bottom**) grids. The **C** state contribution (blue) and **D** state contribution (red) are shown.

included in the vibronic calculations, the vibronic state **C**,43 is still above the dissociation threshold and therefore remains unbound.

Analogous to the adiabatic only calculations, the squared contributions of the nonadiabatically coupled probability densities from the **C** (shown in blue) and the **D** (shown in red) adiabats are shown in Fig. S14 and Fig. S15. Since the zeroth-order **D**,0 vibrational state is embedded in the bound manifold of zeroth-order **C** states, when nonadiabatically coupled linear combinations are formed. The largest mixing occurs between **D**,0 and **C**,41 creating mixed states with primarily **C**,41 character (see Fig. S14 middle, right) and primarily **D**,0 character (see Fig. S15 top, left). The most significant difference between the truncated and extrapolated grids is that a fairly substantial mixing occurs in the state with primarily **C**,42 character (see Fig. S14 bottom, right) on the truncated grid that is less coupled on the extrapolated grid. On the extrapolated grid it is evident that states with primarily **D**,1 and greater character are coupled to **C** states in the dissociation continuum and are therefore unbound.

References

(1) T. H. Dunning Jr, *J. Chem. Phys.*, 1989, **90**, 1007–1023.

(2) M. Aymar, J. Deiglmayr and O. Dulieu, *Can. J. Phys.*, 2009, **87**, 543–556.

(3) J. Sansonetti, *J. Phys. Chem. Ref. Data*, 2008, **37**, 1659–1763.

(4) S.-D. Walji, K. M. Sentjens and R. J. Le Roy, *J. Chem. Phys.*, 2015, **142**, 044305.

(5) C.-C. Chu, H.-Y. Huang, T.-J. Whang and C.-C. Tsai, *J. Chem. Phys.*, 2018, **148**, 114301.